Interfacial Investigation of Explosion-Welded Titanium/ Steel Bimetallic Plates

Qiaoling Chu, Xiongwei Tong, Shuai Xu, Min Zhang, Jihong Li, FuXue Yan, and Cheng Yan

Commercial pure titanium and low carbon steel were explosive welded. The interfacial structures were examined using a combined microstructural analysis and nanoindentation tests. The interface has a wavy morphology with an isolated mixing zone where a mixing of elemental titanium (Ti) and iron (Fe) occurs. Constituents in the mixing zone vary even under the same explosive welding conditions; for example, some are dominated by Fe_2Ti intermetallics, whereas some consists of Fe_2Ti and FeTi intermetallics. The nanoindentation tests and fracture observation confirm the brittle nature of the Fe-Ti intermetallics that formed in the mixing zone. The FeTi phase ($\sim$ 20.3 GPa) showed higher hardness than the Fe_2Ti phase ($\sim$ 14.2 GPa). Simple approaches to estimate the cooling rate at the Ti/steel interface are proposed, and the calculated rate is 2.1×10^7 K/s. Such a high cooling rate combined with the chemical compositions results in the formation of the nanoscaled Fe_2Ti structure in the mixing zone.

1. Introduction

Developments in advanced technologies are required for new materials to achieve superior properties, such as corrosion and wear resistance for industrial application (Ref 1-3). Titanium-to-steel joining has a high economic and technical interest for many industries. Because of the formation of brittle Fe-Ti intermetallics and thermal-stress mismatching, these metals are difficult to join through fusion welding (Ref 4, 5) and some solid-state joining methods (Ref 6-8). Explosive welding is a common technique to bond virtually any combination of metals (Ref 9-12). Upon detonating the explosive, a fly plate is accelerated across a stand-off distance and collides with the base plate. At the collision point, the pressure (up to 10 GPa) normally exceeds the material yield strength, which results in the materials behaving like a fluid and forming a mixing zone (Ref 13-16). Process parameters, including the collision angle (β) and collision point velocity (V_c), are critical factors that affect the bonding quality (Ref 17). Similar combinations [Fe/Fe (Ref 18), Ti/Ti (Ref 19)] and dissimilar combinations (Al/Fe (Ref 20), Ti/Fe (Ref 21), Ti/Al

(Ref 22), Ni/Fe (Ref 23), Cu/Fe (Ref 24), Al/Mg (Ref 25)) have been explosive cladded.

Because of the severe rapid collision during explosive welding, the formation of structures at the interface, especially in the mixing zone, is far from equilibrium. Nishida et al. (Ref 26) observed Ti_2Ni, TiNi, icosahedral quasicrystals and an amorphous phase in the Ti/Ni mixing zone. These products were concluded to be the trace of melting and subsequent rapid solidification of thin layers along the contact surface of both the parent materials. Fan et al. (Ref 27) demonstrated that a loss of crystalline structure at the bonding interface was driven by lattice collapse during the high-strain-rate impact process and then followed by inter-diffusion reactions at temperatures below the melting point. Song et al. (Ref 28) identified the formation of FeTi and metastable $Fe_{9.64}Ti_{0.36}$ phases in the Ti/ steel mixing zone. Bataev et al. observed the formation of metallic glasses at the interface of austenitic stainless steel and niobium (Ref 29), and the precipitation of decagonal quasicrystals and metastable Ni_2Al_9 crystals at the interface of the explosion-welded Al/Ni plate (Ref 30). Scanning electron microscopy (SEM) and transmission electron microscopy (TEM) were used to characterize the microstructures at the explosive interface. No investigation, however, revealed the mechanical properties of the individual structure at the interface. Compared with conventional mechanical tests, nanoindentation has demonstrated to be a powerful tool for mechanical characterization at a small scale (Ref 31, 32). Our previous study investigated the Ti/steel bimetallic plate quantitatively via nanoindentation tests (Ref 33). The Fe-Ti intermetallics that formed at the Ti/steel interface presented high hardness. These resultant complex microstructures (especially the brittle intermetallics) most probably determine the overall mechanical properties of the cladded structures (Ref 34-36). Although the phenomenon of interfacial structure has been reported widely (Ref 26-29, 33), only a few studies have been devoted to probe the formation mechanism of these brittle structures at the interfaces of explosion-welded materials.

Recently, Bataev et al. (Ref 37) investigated metastable phases at the explosion-welded alloy interface. Heating and cooling rates at the interfaces between the

Qiaoling Chu, College of Materials Science and Engineering, Xi'an University of Technology, Xi'an 710048, China; and School of Chemistry, Physics and Mechanical Engineering, Science and Engineering Faculty, Queensland University of Technology (QUT), Brisbane, QLD 4001, Australia; **Xiongwei Tong, Shuai Xu, Min Zhang, Jihong Li,** and **FuXue Yan**, College of Materials Science and Engineering, Xi'an University of Technology, Xi'an 710048, China; and **Cheng Yan**, School of Chemistry, Physics and Mechanical Engineering, Science and Engineering Faculty, Queensland University of Technology (QUT), Brisbane, QLD 4001, Australia. Contact e-mails: chuqiaoling@xaut.edu.cn and c2.yan@qut.edu.au.

explosion-welded materials were proposed, and the solidification conditions of these phases were analyzed via the cooling rates. These results provided insight into the investigation of the interfacial structures of the explosion-welded alloys.

A combination of two factors, namely, the material composition and its temperature histories, determines the formation of complex structures (metastable phases, nanosized grains and quasicrystals). Our previous work (Ref 33) has simulated the temperature field distributions at the interfacial regions during explosive welding. In this work, the formation mechanism of the interfacial structures at the interfaces of the explosion-welded Ti/steel bimetallic plate was investigated via thorough analysis of the temperature history (especially the cooling rate), microstructure (SEM and TEM) and mechanical properties (nanoindentation and tensile tests). The results could provide a better understanding of the structure–property relationship in the explosion-welded Ti/steel bimetallic structure.

2. Experimental Procedure

A commercial pure Ti plate (Grade 1, thickness ~ 2 mm) was explosive welded to a low-carbon-steel plate (S235, thickness ~ 14 mm) in a parallel stand-off configuration, as shown in Fig. 1. The low-carbon-steel substrate was used as a load-bearing component, whereas the thin commercial pure Ti layer was used to protect the steel in a corrosive environment. The chemical compositions of the base metals are listed in Table 1. The Ti plate consists mainly of an α-Ti structure with an ultimate strength of 460 MPa. The steel plate consists mainly of pearlite and ferrite structures, with an ultimate strength of 360 MPa. The explosive material was an ammonium-nitrate-fuel–oil mixture with a density of 0.92 g/cm^3. The explosive detonation velocity was 2850 m/s, and the impact angle was 15°. The stand-off distance was 20 mm, and the explosive thickness was 20 mm. Specimens for microstructure analysis were prepared from the central part of the joint in a plane parallel to the detonation direction and normal to the explosive interface. Mechanical polishing using grinding papers down to 1200 gird was carried out followed by diamond polishing using 9, 3 and 1 μm diamond slurries. The deformation zone in the surface from previous steps was removed using a 0.04-μm colloidal-silica suspension. A JOEL 7001F SEM with EBSD detector was used to characterize the microstructure

V$_d$—Detonation velocity   V$_p$—Collision velocity
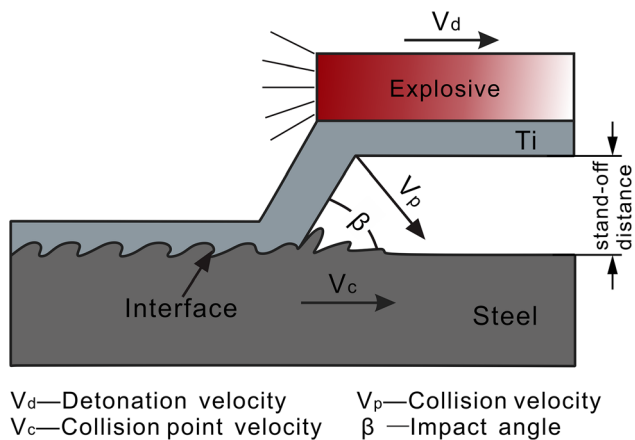V$_c$—Collision point velocity   β —Impact angle

Fig. 1 Schematic of explosive welding

at the explosive interface. TEM observations were carried out using a JEOL 2100 microscopy at 200 kV. The TEM samples were prepared using a FEI Quanta 200 3D dual beam focused ion beam (FIB). X-ray diffraction (XRD) patterns were collected on the cross sections and the fracture surfaces (after tensile tests) using a Rigaku-binary diffractometer (Rigaku SmartLab) with a Cu target. Patterns were collected with a step size of 0.05°. Nanoindentation was conducted using a Berkovich indenter (Hysitron Triboindenter TL-950) with a load-control mode. A maximum load of 3 mN with a constant loading rate of 400 μN/s was set. Fused quartz with a known Young's modulus (69.6 GPa) and hardness (9.25 GPa) was calibrated for the tip area function. An array with 80 indents (8 × 10) was set on the sample. The measured hardness of each phase was averaged from at least three indentations. Specimens for the standard flat tensile tests were extracted from the central part of the bimetallic plate with the longitudinal axis parallel to the explosive welding direction, as shown in Fig. 2. Tensile tests were carried out at room temperature at a crosshead speed of 1 mm/min, and the fracture morphology was observed by SEM.

3. Results

3.1 Microstructures

Figure 3(a) shows the typical wavy structure at the Ti/steel interface. The wavelength and amplitude are ~ 800 μm and 180 μm, respectively. During explosive welding, the circular movement and intense stirring in the vortexes lead to Ti and Fe materials mixing, as shown in Fig. 3(b) and (c). The mechanical energy during rapid pressurization converts to heat accumulation, which melts the Ti and Fe materials and forms a mixing zone (indicated by red arrows in Fig. 3a). Figure 3(d) shows the concentration profiles of the elemental Fe and Ti across the mixing zone, which suggest a sharp transition near the interface of each base metal and a relevant uniform distribution (Fe ~ 76.3 at.%, Ti ~ 23.7 at.%) in the mixing zone. Generally, a wavy interface is preferred because it increases the bond area and produces a greater depth of shock hardening, which provides stronger bonding. The interface contributes to isolating the trapped jetting, which leads to the formation of an isolated mixing zone in front of each wave.

To characterize the phases that may form in the mixing zone, EBSD analysis was conducted for a selected mixing zone (Fig. 4a). Figure 4(b) is the inverse pole figure (IPF) of region b, where the Fe base metal and partial mixing zone are involved. With the corresponding phase map (Fig. 4c), the mixing zone is dominated by Fe$_2$Ti intermetallics. A layer with much finer Fe grains (< 1 μm) formed between the Fe base metal and the mixing zone, as indicated by white arrows. According to our previous study (Ref 33), the fine Fe grains are most probably recrystallization structures. The extreme temperatures, which normally reach the melting point of the base metals, and pressures in the regions nearest the mixing zone, promote dynamic recrystallization in the severely deformed grains (Ref 33, 38).

The grain size of these Fe$_2$Ti intermetallics varies (Fig. 4d and e), that is, region d shows finer Fe$_2$Ti grains (1-2 μm), whereas region e shows much coarser grains (~ 10 μm). During explosive welding, the temperature of the materials that

Table 1 Chemical compositions of applied materials (wt.%)

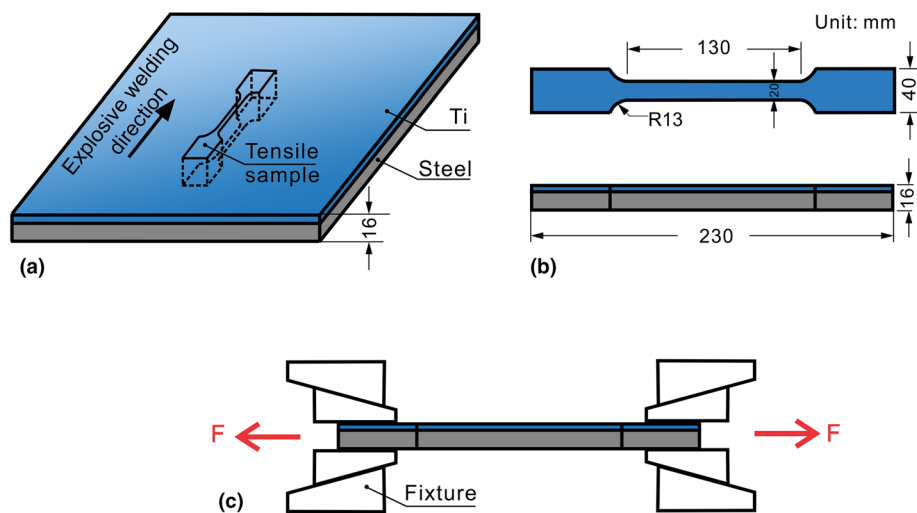|	C	Si	Mn	Ti	Cu	Fe	V	O	N	H
Ti (grade 1)	0.10	...	...	Bal.	...	0.25	...	0.20	0.03	0.015
Steel (S235)	0.12	0.30	0.50	...	...	Bal.	...	...	...	...

Fig. 2 Illustration of tensile sample used to examine the mechanical properties of the Ti/steel bimetallic plate. (a) Location of fabricated tensile sample; (b) dimensions of tensile sample; (c) schematic of tensile tests

surround the collision point could reach the melting point. Region d close to the Fe and Ti base metals experiences a higher cooling rate than region e (in the center of the mixing zone), which could suppress grain growth to some extent. The Fe_2Ti grain size presented here is much coarser than that observed in our previous work (Ref 33) for the CP-Ti/Q345 bimetallic plate. The cracks in this selected mixing zone imply the brittle nature of these Fe_2Ti intermetallics.

To determine the microstructure distributions in the mixing zone, TEM lamella were prepared by FIB, shown in Fig. 5(a) and (b). Figure 5(c) and (d) presents the TEM bright-field contrast images and corresponding diffraction patterns. FeTi intermetallics with a maximum grain size of $\sim$ 200 nm are distributed among the Fe_2Ti matrix grains in Fig. 5(c). Some nanoscaled Fe_2Ti grains (identified by TEM-EDS analysis) are visible, as indicated by red arrows in Fig. 5(e). Nanoscaled FeTi intermetallics are visible here, whereas they are not present in the EBSD phase map in 4c, most likely because of the lower-resolution EBSD method. Some researchers have reported amorphous phases that formed at the Ti/steel interface (Ref 39, 40). However, these phases are not observed here. Fe-Ti alloys do not have high glass-formation abilities. Even near eutectic compositions, Fe-Ti amorphous phases are rarely obtained under rapid cooling experiments (Ref 41, 42). Minor additions of alloying elements in titanium and steel could enhance the glass-formation abilities and promote glass formation (Ref 43). The alloy content in the base metals (low carbon steel and commercial pure titanium in Table 1) is relatively low, which may be responsible for the absence of amorphous phases in the mixing zone.

The XRD pattern on the Ti/steel cross sections confirms the presence of Fe_2Ti and FeTi intermetallic phases, as shown in Fig. 6(a). After tensile tests, the Ti side and steel side are separated. Figure 6(b) is obtained on the fracture surfaces (at the Ti side) after the tensile tests, which also identifies similar phase constituents.

3.2 Nanoindentation

A grid with 80 points, as outlined by a dashed white rectangle in Fig. 7(a), was subjected to nanoindentation tests. Figure 7(b) shows the corresponding hardness contour profiles. Most of the mixing zone presents a uniform hardness contour (9-13 GPa), whereas the region near the Fe base metal shows higher hardness (indicated by a red contour in Fig. 7b), from 17 to 22 GPa. With the EDS analysis, this region consists mainly of FeTi intermetallics (Fe $\sim$ 57.2 at.%, Ti $\sim$ 42.8 at.%), whereas the remaining region consists of Fe_2Ti intermetallics (Fe $\sim$ 23.3 at.%, Ti $\sim$ 76.7 at.%). Figure 7(c) and (d) displays representative Berkovich impressions (marked by a yellow rectangle in Fig. 7a) and an EBSD phase map, respectively. FeTi and α-Fe have similar crystalline parameters, which make it difficult to distinguish them under a EBSD detector. Therefore, only the crystal lattice of the α-Fe phase is input for EBSD analysis. The region with higher hardness is dark gray, whereas the other region is light gray. As shown in Fig. 7(c), the FeTi ($\sim$ 20.3 GPa) and Fe_2Ti ($\sim$ 14.2 GPa) have smaller indents than the Fe base metal ($\sim$ 2.2 GPa). The force–displacement (P–h) curves for these typical phases are plotted in Fig. 6(e). The maximal indenter displacement with a peak load of 3 mN is 81.7 and 97.8 nm in the FeTi and Fe_2Ti phases, respectively.

In practice, particularly when large workpieces are joined, collision parameters may change during welding because of the gap variability or inhomogeneity of the explosives. Thus, within the same explosion-welded plate, different structures
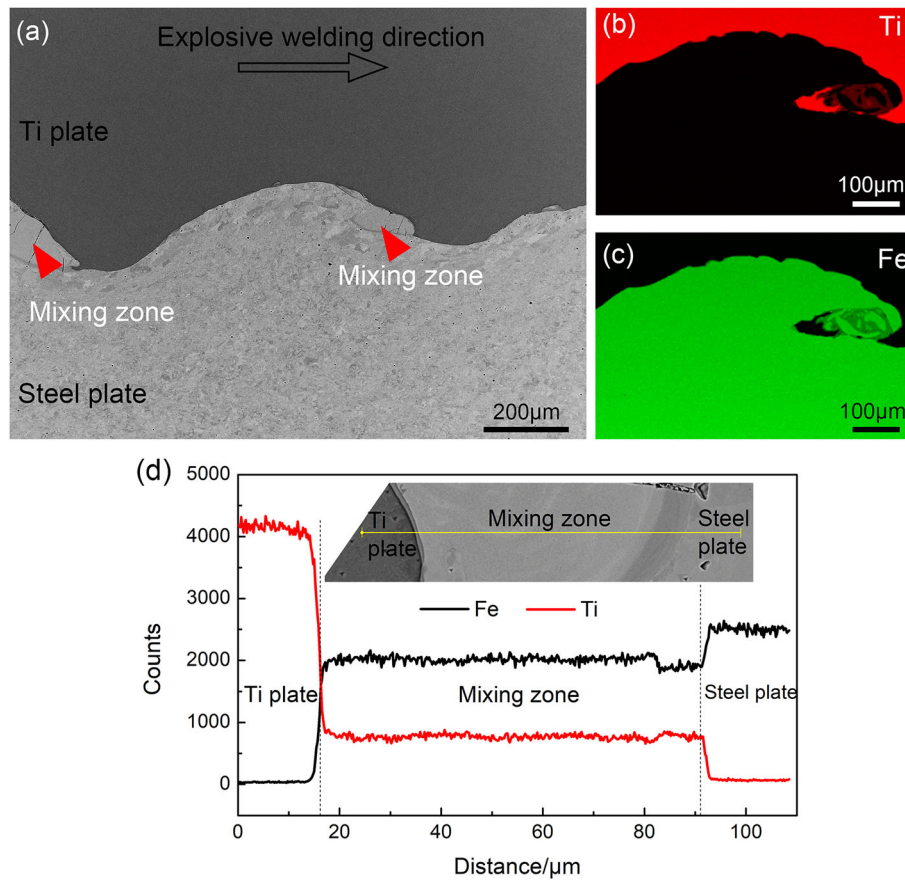
Fig. 3 Backscattered electron image (BSE) on cross section of Ti/steel explosion-bonded joint. (a) Typical wave morphology with mixing zone formed in front of each wave; (b) and (c) chemical composition distributions of elemental Ti and Fe in one wave, respectively; (d) EDS line scanning across the mixing zone

may be observed. Even in the same wave structure, the interfacial structures do not show uniform distribution along the interface. The above factors could be responsible for the different intermetallic constituents and grain sizes in Fig. 4 and 7.

3.3 Fracture Analysis

Figure 8(a) shows the force–displacement curve of the Ti/steel bimetallic joint in the tensile tests. The ultimate tensile strength is 432 MPa. Because the base metals (Ti and steel) have a significant difference in strength and ductility, the 2-mm-thick Ti plate fails first, and then the explosive interface separates. With an increase in displacement, the steel plate (thickness $\sim$ 14 mm) fails. If we consider the ultimate stress and cross section of each plate, the fracture force of the Ti plate is $\sim$ 18400 N (460 MPa $\times$ 20 mm $\times$ 2 mm), whereas that of the steel plate is $\sim$ 100800 N (360 MPa $\times$ 20 mm $\times$ 14 mm). Because the fracture force of the Ti plate is much lower than that of the steel plate, the influence of the fracture of the Ti plate is negligible during the tensile tests. Therefore, the force–displacement curve looks smooth without any indication of intermediate failure in the individual component.

After the tensile tests, the Ti side was selected for fractography analysis, as indicated by the inset. The Ti base metal is dominated by dimple morphology, as shown in Fig. 8(b). However, a cleavage morphology is observed at the explosive interface (Fig. 8c). EDS analysis (Fe $\sim$ 72.5 at.%,

Ti $\sim$ 27.5 at.%) identifies blocky breaking that is composed mainly of Fe_2Ti intermetallics. The fracture morphology determines the brittle nature of the Fe_2Ti phase, which is consistent with the nanoindentation results.

4. Discussion

During explosive welding, material heating in some volume that surrounds the collision point occurs because of a significant increase in pressure and plastic flow in this area, as shown in Fig. 9(a) and (b) (Ref 37). The velocity of the collision point, V_c, governs the time available for bonding. These two schematic diagrams describe the flat interface with a continuous mixing zone that formed in a similar materials combination. Ti/steel explosive interface is featured by a wave morphology with an isolated mixing zone. The characteristic deformation during explosive welding is shown in Fig. 9(c), where the mixing zone, severely deformed zone and slightly deformed zone are identified with different effective plastic strains (Ref 33). The region with 100% strain consists of the mixing zone and severe deformation zone. For the Ti/steel dissimilar joint, the deformation region is asymmetrical.

As the collision point moves forward, material in the high-pressure zone starts cooling because of heat transfer to the adjacent region. It is assumed that deformation during explosive welding is adiabatic, and by the time the cooling begins,
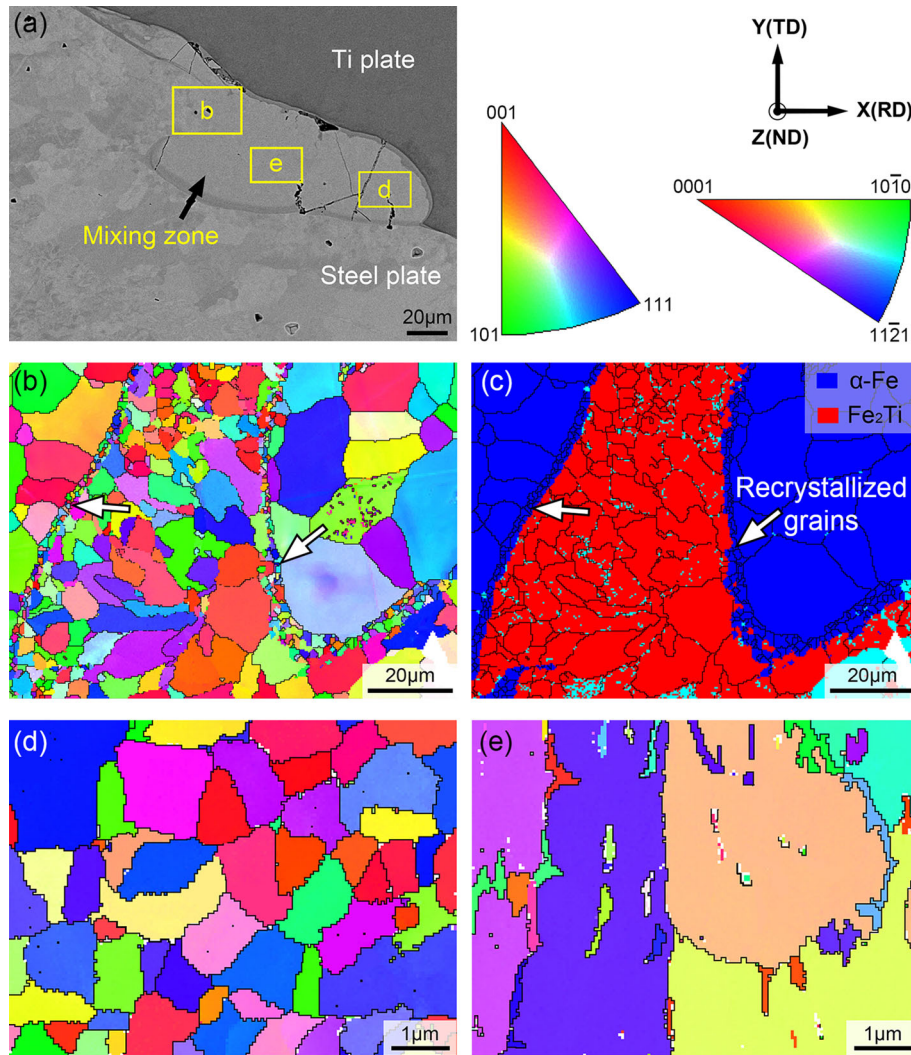
Fig. 4 EBSD results of mixing zone. (a) BSE image that indicates regions selected for EBSD analysis; (b), (d) and (e) EBSD IPFs in region b, d and e, respectively; (c) EBSD phase map in region b

the deformation process has ended. In (Ref 44, 45), the solidification time (t_s) of the molten metal must be lower than the time needed for a positive pressure (t_p) at the interface. The expressions that are proposed to estimate t_p and t_s are obtained from (Ref 44, 45):

$$t_p = \left[0.5 + 0.66 \left(\frac{\rho_{fly} \cdot V_c^2}{G_{fly}} \right) \right] \cdot \frac{\delta_{fly}}{V_c}$$

$$t_s = \frac{Q^2}{4\pi \cdot c_{fly} \cdot \lambda_{fly} \cdot \rho_{fly} \cdot T_{mfly}^2} \tag{Eq 1}$$

$$Q = 6.8 \cdot 10^{-2} \cdot V_c^2 \cdot \rho_{fly} \cdot \delta_{fly} \cdot \frac{\delta_{base}}{\delta_{fly} + \delta_{base}} \cdot \sin^2 \left(\frac{\beta}{2} \right) \tag{Eq 2}$$

where, ρ_{fly}, G_{fly}, V_c, δ_{fly}, c_{fly}, λ_{fly} and T_{mfly} are the density, shear modulus, collision point velocity, thickness, specific heat, thermal conductivity and melting point of the fly plate, respectively; Q is the heat released at the interface; δ_{base} is the thickness of the base plate and β is the collision angle.

ρ_{fly} is 4.5 kg/m³, G_{fly} is 55 GPa, V_c is 2850 m/s, δ_{fly} is 2 mm, δ_{base} is 14 mm, λ_{fly} is 15 Wm⁻¹ k⁻¹, c_{fly} is 523 J kg⁻¹ K⁻¹, T_{mfly} is 1670 °C and β is 15°.

The calculated t_p and t_s for the Ti/steel joint are 0.81 and 0.09 μs, respectively. The above criterion is reliable for joints that are welded by ammonium-nitrate-fuel–oil explosion. The above expressions are developed for similar materials welding, where the formation of intermetallic phases usually does not occur. Because intermetallics are formed at the Ti/steel interface, one may suggest a consideration of the physical properties of these phases to obtain a more accurate solidification time. However, information on the physical properties of these intermetallics (FeTi and Fe₂Ti) is limited. Furthermore, the mixing zone is not fully homogeneous. Therefore, an accurate analysis of the solidification time when considering the intermetallics in the mixing zone cannot be made. Results in Ref 46, 47 suggest that these two equations are suitable for dissimilar materials welding when the interfacial mixing zone is thin. If the interfacial mixing zone is thick, Eq 2 will be invalid. In this study, the Fe-Ti intermetallics that formed at the Ti/steel interface are isolated (mixing zone in Fig. 3). The t_s (90 ns) that is calculated here is similar to that reported in Ref 19, which proves the applicability of Eq 2 in a Ti/steel dissimilar joint. Therefore, Eq 2 can be adapted to estimate the solidification time (t_s). These two expressions indicate that an increase in fly-
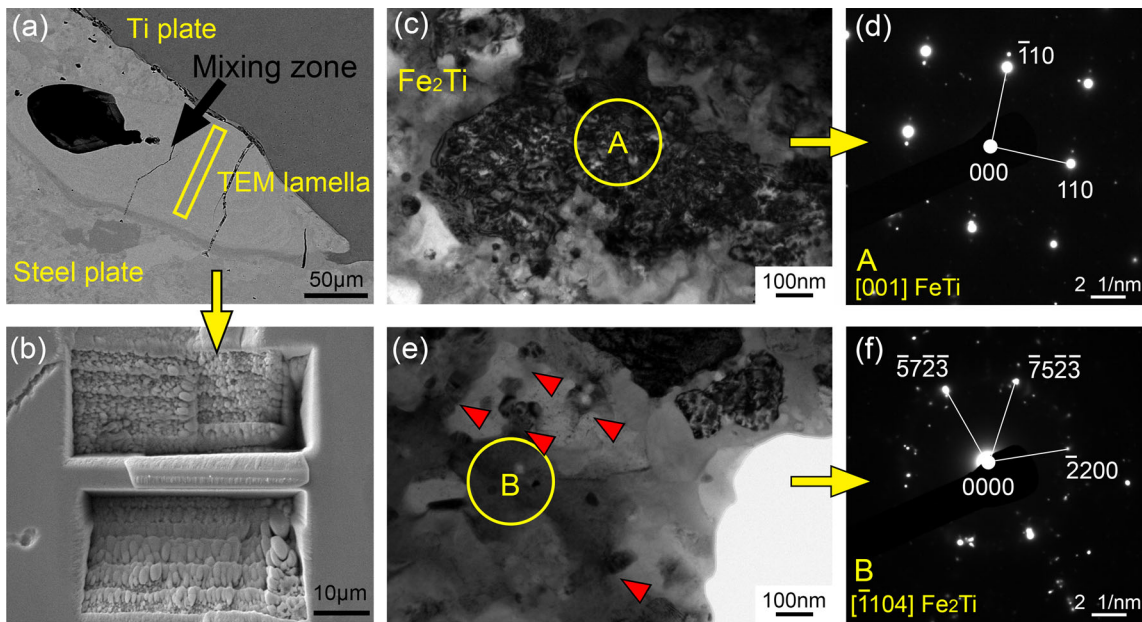
Fig. 5 TEM bright-field images of mixing zone. (a) and (b) TEM lamella preparation by FIB; bright-field images of (c) FeTi and (e) Fe$_2$Ti intermetallics phases, respectively; electron-diffraction patterns showing (d) FeTi and (f) Fe$_2$Ti intermetallic phases, respectively. Size of selected area aperture was ∼ 200 nm
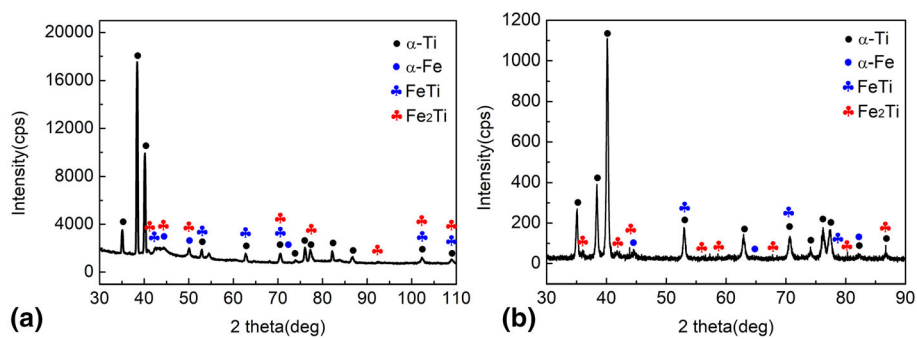

Fig. 6 XRD pattern at the Ti/steel interface. (a) On cross sections before tensile tests; (b) on the fracture surfaces of Ti side after tensile tests

plate thickness increases the solidification time t_s. Kuz'min et al. (Ref 47) proposed a critical thickness of the fly plate in explosive welding materials with greatly different properties (such as aluminum and steel).

Around the collision point, conditions of a perfect thermal contact are established immediately between the liquid (mixing zone) and the solid (Ti and steel base metals). In the mixing zone, possible phase transformations occur, that is, L → Fe$_2$Ti, ∼ 1427 °C; L + Fe$_2$Ti → FeTi, ∼ 1317 °C (Ref 48). Subsequent cooling occurs by heat transfer from the interfacial area to the severely deformed zone. Based on the time calculated by Eq 1 and 2, the averaged cooling rate reaches 2.1×10^7 K/s. This value is consistent with those in Ref 37. Such a high cooling rate results in material quenching in the mixing zone. Heat transfer leads to recrystallization in the deformed grains (fine Fe grains in Fig. 4b). Several research works have reported the amorphous (Ref 27), quasi-crystal (Ref 49) and nanoscaled structures (Ref 33) that formed in the mixing zone. The formation of these structures is determined by two factors-material compositions and temperature history, which explains the different phases observed at the Ti/steel

interface. Another consequence of a high cooling rate is the significant heterogeneity of the compositions across the volume of the mixing zone (shown in Fig. 7d). Although element mixing occurs in the liquid state, the time for the liquid-phase existence is insufficient to complete diffusion and homogenize the compositions.

In the dissimilar welding of metals with a high affinity to form intermetallic phases (such as Ti/Fe, Al/Fe combinations), the welding quality is influenced by the properties of the welded metals, and the physical properties of the new phases that formed at the interface. Crossland et al. (Ref 16) proved that these new phases will not affect the properties of the explosion-welded joints significantly if they do not form a continuous layer at the interface, but rather, form a separate "island." During explosive welding, the fly plate collides toward the base plate at an extremely high velocity. The residual stress at the bonding interface may be high. However, few researchers have focused on this aspect. Therefore, our future research will characterize the residual stress distribution at the explosive interface with different methods (Ref 50).
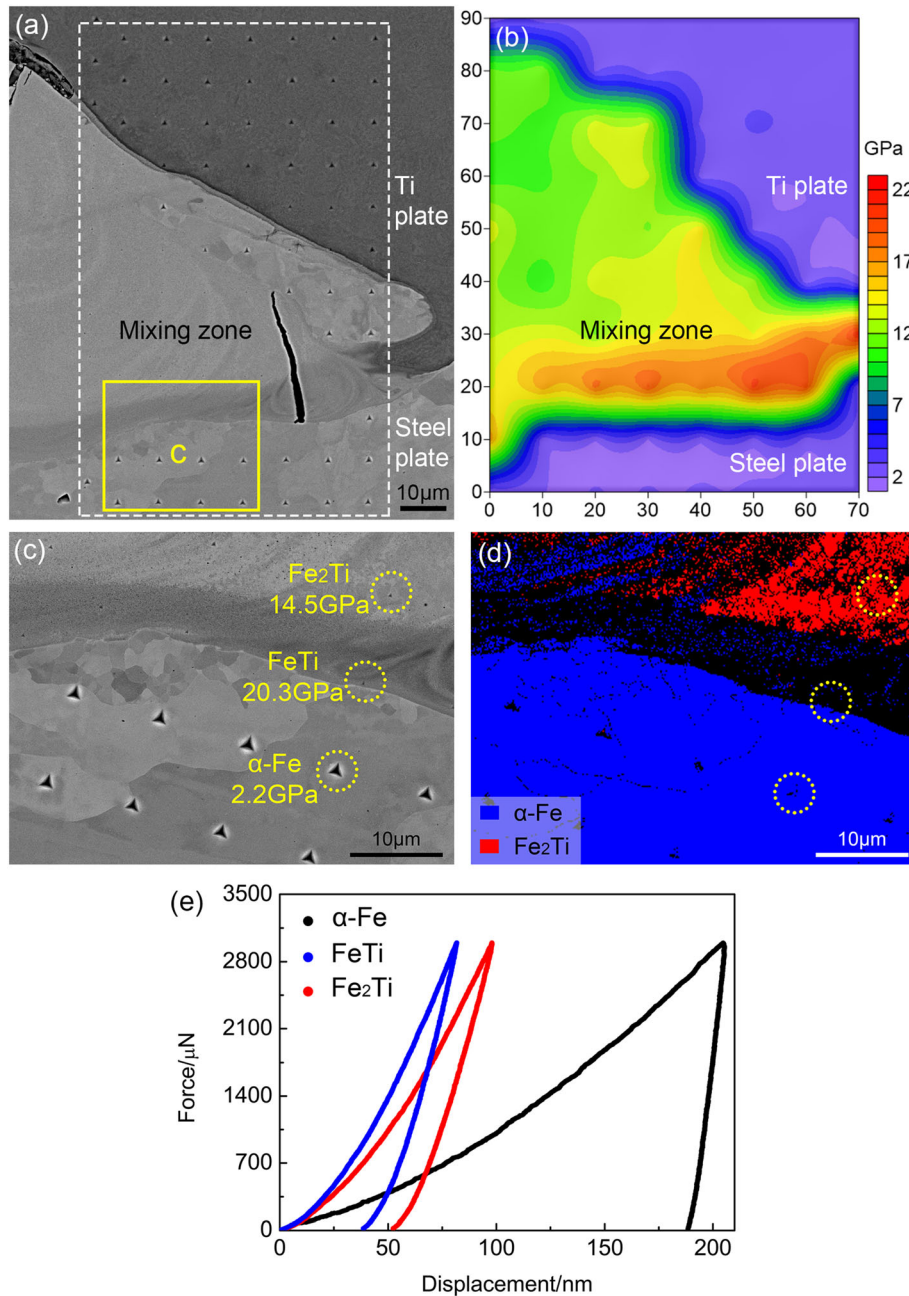
Fig. 7 Nanoindentation tests on cross section of Ti/steel joint. (a) Low-magnification BSE image highlighting tested area; (b) hardness contour profiles; (c) BSE image and (d) EBSD phase map of selected region, respectively; (e) force–displacement (P–h) curves for typical phases

5. Conclusions

The microstructure and mechanical properties of explosion-welded Ti/steel bimetallic plate were investigated. The explosive interface was characterized by a typical wave structure with a mixing zone that was isolated in each wave. The mixing zone was dominated by Fe-Ti intermetallics. FeTi ($\sim$ 20.3 GPa) and Fe_2Ti ($\sim$ 14.2 GPa) showed higher hardness than the Fe base metal ($\sim$ 2.2 GPa). The resultant Ti/steel bimetallic joint had an ultimate strength of 432 MPa. A cleavage morphology was observed at the explosive interface. Simple approaches were applied to estimate the cooling rate at Ti/steel interface, and the calculated value was 2.1×10^7 K/s. Such a high cooling rate with the chemical compositions resulted in the formation of a nanoscaled Fe_2Ti structure in the mixing zone.
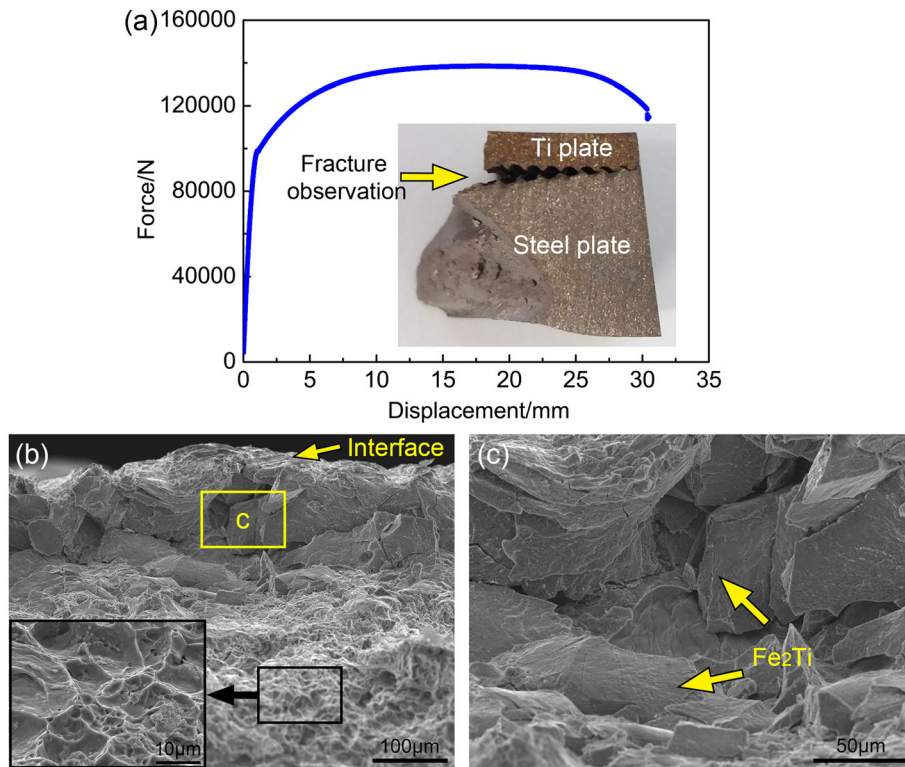
Fig. 8 Tensile test results. (a) Force–displacement curve; (b) dimple morphology at Ti side; (c) cleavage morphology at explosive interface
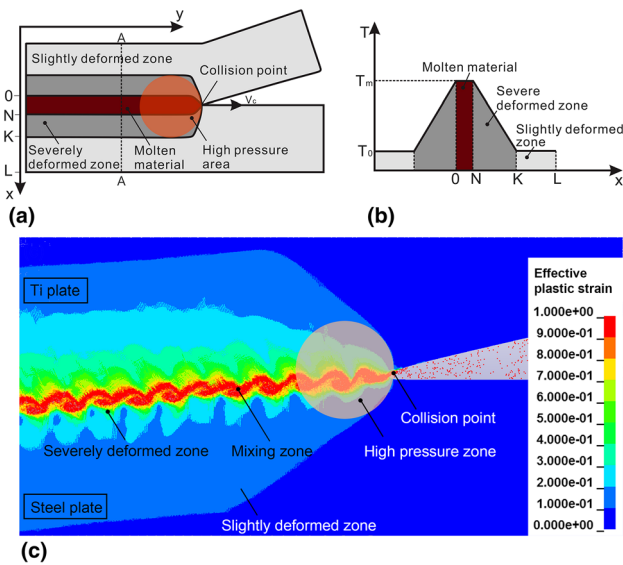

Fig. 9 (a) Schematic diagram for formation of a flat interface with a continuous mixing zone along the interface during explosive welding of a similar metal combination; (b) simplified schematic diagram of temperature distribution across section A–A immediately after completion of heating (reprinted from Ref 37, with permission), (c) numerical results of effective plastic strain along Ti/steel interface during explosive welding (reprinted from Ref 33, with permission)

Data availability

The processed data required to reproduce these findings cannot be shared at this time because of legal or ethical reasons. The processed data required to reproduce these findings cannot be shared at this time because of technical or time limitations. The processed data required to reproduce these findings cannot be shared at this time as the data form part of an ongoing study.

References

1. J. Yang, Z.S. Yu, Y.L. Li, H. Zhang, and N. Zhou, Laser Welding/ Brazing of 5182 Aluminium Alloy to ZEK100 Magnesium Alloy Using a Nickel Interlayer, *Sci. Technol. Weld. Join.*, 2018, **7**, p 543–550

2. L.J. Zhang, C.H. Wang, Y.B. Zhang, Q. Guo, R.Y. Ma, J.X. Zhang, and S.J. Na, The Mechanical Properties and Interface Bonding Mechanism of Molybdenum/SUS304L by Laser Beam Welding with Nickel Interlayer, *Mater. Des.*, 2019, **182**, p 108002

3. Y.L. Li, Y.R. Liu, and J. Yang, First Principle Calculations and Mechanical Properties of the Intermetallic Compounds in a Laser Welded Steel/Aluminum Joint. Opt. Laser Technol. 122, 105875 (2020)

4. I. Tomashchuk, D. Grevey, and P. Sallamand, Dissimilar Laser Welding of AISI, 316L Stainless Steel to Ti6-Al4-6 V Alloy Via Pure Vanadium Interlayer, *Mater. Sci. Eng. A*, 2015, **622**, p 37–45

5. T. Wang, B.G. Zhang, H.Q. Wang, and J.C. Feng, Microstructures and Mechanical Properties of Electron Beam-Welded Titanium-Steel Joints with Vanadium, Nickel, Copper and Silver Filler Metals, *J. Mater. Eng. Perform.*, 2014, **23**, p 1498–1504

6. S.H. Li, Y.H. Chen, J.D. Kang, Y.D. Huang, J.A. Gianetto, and L.M. Yin, Interfacial Microstructures and Mechanical Properties of Dissimilar Titanium Alloy and Steel Friction Stir Butt-Welds, *J. Manuf. Process.*, 2019, **40**, p 160–168

7. C. Velmurugan, V. Senthilkumar, S. Sarala, and J. Arivarasan, Low Temperature Diffusion Bonding of Ti-6Al-4 V and Duplex Stainless Steel, *J. Mater. Process. Technol.*, 2016, **234**, p 272–279

8. S. Kundu, S. Sam, and S. Chatterjee, Evaluation of Interface Microstructure and Mechanical Properties of the Diffusion Bonded Joints of Ti-6Al-4 V Alloy to Micro-Duplex Stainless Steel, *Mater. Sci. Eng. A*, 2011, **528**, p 4910–4916

9. F. Findik, Recent Developments in Explosive Welding, *Mater. Des.*, 2011, **32**, p 1081–1093

10. N.N. Gou, L.J. Zhang, and J.X. Zhang, Increased Quality and Welding Efficiency of Laser Welding of 2205/X65 Bimetallic Sheets with a Lagging MIG Arc, *J. Mater. Process. Technol.*, 2018, **251**, p 83–92

11. J. Ning, L.J. Zhang, M.X. Xie, H.X. Yang, X.Q. Yin, and J.X. Zhang, Narrow Gap Multi-Pass Laser Butt Welding of Explosion Welded CP-Ti/Q235B Bimetallic Sheet by Using a Copper Interlayer, *J. Alloys Compd.*, 2017, **698**, p 587–602

12. T. Wang, F. Zhang, X.P. Li, S.Y. Jiang, and J.C. Feng, Interfacial Evolution of Explosively Welded Titanium/Steel Joint Under Subsequent EBW Process, *J. Mater. Process. Technol.*, 2018, **261**, p 24–30

13. G.H.S.F.L. Carvalho, R. Mendes, R.M. Leal, I. Galvão, and A. Loureiro, Effect of the Flyer Material on the Interface Phenomena in Aluminium and Copper Explosive Welds, *Mater. Des.*, 2017, **122**, p 172–183

14. I.A. Bataev, A.A. Bataev, V.I. Mali, V.G. Burov, and E.A. Prikhod'ko, Formation and Structure of Vortex Zones Arising Upon Explosion Welding of Carbon Steels, *Phys. Met. Metallogr.*, 2012, **113**(3), p 233–240

15. Y.X. Wang, H.G. Beom, M. Sun, and S. Lin, Numerical Simulation of Explosive Welding Using the Material Point Method, *Int. J. Impact Eng.*, 2011, **38**, p 51–60

16. B. Crossland and A.S. Bahrani, Fundamentals, of Explosive Welding, *Contemp. Phys.*, 1968, **9**(1), p 71–87

17. S.A.A. Akbari Mousavi, S.T.S. Al-Hassani, and A.G. Atkins, Bond Strength of Explosively Welded Specimens, *Mater. Des.*, 2008, **29**, p 1334–1352

18. L.J. Zhang, Q. Pei, J.X. Zhang, Z.Y. Bi, and P.C. Li, Study on the Microstructure and Mechanical Properties of Explosive Welded 2205/X65 Bimetallic Sheet, *Mater. Des.*, 2014, **64**, p 462–476

19. Y.S. Fu, M. Xia, and Z. Wang, Quantitative Evaluation for Structure Difference Between Central Region and Periphery in Al-Al Explosive Welding Interface, *Rare Met. Mater. Eng.*, 2017, **46**(7), p 1827–1832

20. G.H.S.F.L. Carvalho, I. Galvão, R. Mendes, R.M. Leal, and A. Loureiro, Formation of Intermetallic Structures at the Interface of Steel-To-Aluminium Explosive Welds, *Mater. Charact.*, 2018, **142**, p 432–442

21. P. Manikandan, K. Hokamoto, M. Fujita, K. Raghukandan, and R. Tomoshige, Control of Energetic Conditions by Employing Interlayer of Different Thickness for Explosive Welding of Titanium/304 Stainless Steel, *J. Mater. Process. Technol.*, 2008, **195**, p 232–240

22. H.B. Xia, S.G. Wang, and H.F. Ben, Microstructure and Mechanical Properties of Ti/Al Explosive Cladding, *Mater. Des.*, 2014, **56**, p 1014–1019

23. H.R. Zareie Rajani and S.A.A. Akbari Mousavi, The Effect of Explosive Welding Parameters on Metallurgical and Mechanical Interfacial Features of Inconel 625/Plain Carbon Steel Bimetallic Plate, *Mater. Sci. Eng. A*, 2012, **556**, p 454–464

24. H. Zhang, K.X. Jiao, J.L. Zhang, and J.P. Liu, Experimental and Numerical Investigations of Interface Characteristics of Copper/Steel Composite Prepared by Explosive Welding, *Mater. Des.*, 2018, **154**, p 140–152

25. S.H. Ghaderi, A. Mori, and K. Hokamoto, Analysis of Explosively Welded Aluminum-AZ31 Magnesium Alloy Joints, *Mater. Trans.*, 2008, **49**(5), p 1142–1147

26. M. Nishida, A. Chiba, Y. Morizono, M. Matsumoto, T. Murakami, and A. Inoue, Formation of Nonequilibrium Phases at Collision Interface in an Explosively Welded Ti/Ni/Clad, *Mater. Trans.*, 1995, **36**(11), p 1338–1343

27. Z.S. Fan, H.P. Yu, and C.F. Li, Interface and Grain-Boundary Amorphization in the Al/Fe Bimetallic System During Pulsed-Magnetic-Driven Impact, *Scr. Mater.*, 2016, **110**, p 14–18

28. J. Song, A. Kostka, M. Veehmayer, and D. Raabe, Hierarchical Microstructure of Explosive Joints: Example of Titanium to Steel Cladding, *Mater. Sci. Eng. A*, 2011, **528**, p 2641–2647

29. I.A. Bataev, K. Hokamoto, H. Keno, A.A. Bataev, I.A. Balagansky, and A.V. Vinogradov, Metallic Glass Formation at the Interface of Explosively Welded Nb and Stainless Steel, *Met. Mater. Int.*, 2015, **21**(4), p 713–718

30. I.A. Bataev, T.S. Ogneva, A.A. Bataev, V.I. Mali, M.A. Esikov, D.V. Lazurenko, Y. Guo, and A.M. Jorge, Jr., Explosively Welded Multilayer Ni-Al Composites, *Mater. Des.*, 2015, **88**, p 1082–1087

31. W. Godoi, N.K. Kuromoto, A.S. Guimaraes, and G.M. Lepienski, Effect of the Hydrogen Outgassing Time on the Hardness of Austenitic Stainless Steels Welds, *Mater. Sci. Eng. A*, 2003, **354**, p 251–256

32. J. Vannod, M. Bornert, J.E. Bidaux, L. Bataillard, A. Karimi, J.M. Drezet, M. Rappaz, and A. Hessler-Wyser, Mechanical and Microstructural Integrity of Nickel-Titanium and Stainless Steel Laser Joined Wire, *Acta Mater.*, 2011, **59**, p 6538–6546

33. Q.L. Chu, M. Zhang, J.H. Li, and C. Yan, Experimental and Numerical Investigation of Microstructure and Mechanical Behavior of Titanium/Steel Interfaces Prepared by Explosive Welding, *Mater. Sci. Eng. A*, 2017, **689**, p 323–331

34. P. Parchuri, S. Kotegawa, H. Yamamoto, K. Ito, A. Mori, and K. Hokamoto, Benefits of Intermediate-Layer Formation at the Interface of Nb/Cu and Ta/Cu Explosive Clads, *Mater. Des.*, 2019, **166**, p 107610

35. D.M. Fronczek, J. Wojewoda-Budka, R. Chulist, A. Sypien, A. Korneva, Z. Szulc, N. Schell, and P. Zieba, Structural Properties of Ti/Al Clads Manufactured by Explosive Welding and Annealing, *Mater. Des.*, 2016, **91**, p 80–89

36. W.S. Park, C.S. Chun, M.S. Han, M.H. Kim, and J.M. Lee, Comparative Study on Mechanical Behavior of Low Temperature Application Materials for Ships and Offshore Structures: Part I-Experimental Investigations, *Mater. Sci. Eng. A*, 2011, **528**, p 5790–5803

37. I.A. Bataev, D.V. Lazurenko, S. Tanaka, K. Hokamoto, A.A. Bataev, Y. Guo, and A.M. Jorge, Jr., High Cooling Rates and Metastable Phases at the Interfaces of Explosively Welded Materials, *Acta Mater.*, 2017, **135**, p 277–289

38. N. Sridharan, P. Wolcott, M. Dapino, and S.S. Babu, Microstructure and Texture Evolution in Aluminum and Commercially Pure Titanium Dissimilar Welds Fabricated Using Ultrasonic Additive Manufacturing, *Scr. Mater.*, 2016, **117**, p 1–5

39. M. Nishida, A. Chiba, Y. Honda, J.-I. Hirazumi, and K. Horikiri, Electron Microscopy Studies of Bonding Interface in Explosively Welded Ti/steel Clads, *ISIJ Int.*, 1995, **35**(2), p 217–219

40. H. Paul, J. Morgiel, T. Baudin, F. Brisset, M. Prazmowski, and M. Miszczyk, Characterization of Explosive Welded Joints by TEM and SEM/EBSD, *Arch. Metall. Mater.*, 2014, **59**(3), p 1129–1136

41. G.C. Pettan, C.R.M. Afonso, and J.E. Spinelli, Microstructure Development and Mechanical Properties of Rapidly Solidified Ti-Fe and Ti-Fe-Bi Alloys, *Mater. Des.*, 2015, **86**, p 221–229

42. I. Levi and D. Shechtman, The Microstructure of Rapidly Solidified Ti-32 wt% Fe Melt-Spun Ribbon, *J. Mater. Sci.*, 1990, **25**, p 1509–1512

43. Y. Guo, I. Bataev, K. Georgarakis, A.M. Jorge, Jr., R.P. Nogueira, M. Pons, and A.R. Yavari, Ni- and Cu-free Ti-Based Metallic Glasses with Potential Biomedical Application, *Intermetallics*, 2015, **63**, p 86–96

44. I.D. Zakharenko, Critical Conditions in Detonation Welding, *Combust. Explos. Shock Waves*, 1972, **8**(3), p 422–427

45. V.V. Efremov and I.D. Zakharenko, Determination of the Upper Limit to Explosive Welding, *Combust. Explos. Shock Waves*, 1976, **12**(2), p 255–260

46. S. Saravanan and K. Raghukandan, Thermal Kinetics in Explosive Cladding of Dissimilar Metals, *Sci. Technol. Weld. Join.*, 2012, **17**(2), p 99–103

47. V.I. Kuz'min, V.I. Lysak, A.N. Kriventsov, and M.A. Yakovlev, Critical Conditions of the Formation and Failure of Welded Joints in Explosive Welding, *Weld. Int.*, 2004, **18**(3), p 223–227

48. G. Cacciamani, J. De Keyzer, R. Ferro, U.E. Klotz, J. Lacaze, and P. Wollants, Critical Evaluation of the Fe-Ni, Fe-Ti and Fe-Ni-Ti Alloy Systems, *Intermetallics*, 2006, **14**, p 1312–1325

49. C. Dong, Z.K. Hei, L.B. Wang, Q.H. Song, Y.K. Wu, and K.H. Kuo, A new Icosahedral Quasicrystal in Rapidly Solidified FeTi$_2$, *Scr. Metall.*, 1986, **20**(8), p 1155–1158

50. C. Liu, Y. Yan, X.H. Cheng, C.J. Wang, and Y. Zhao, Residual Stress in a Restrained Specimen Processed by Post-Weld Ultrasonic Impact Treatment, *Sci. Technol. Weld. Join.*, 2019, **24**, p 193–199